N O T E

Magnetic Resonance in Medicine

In vivo demonstration of microscopic anisotropy in the human kidney using multidimensional diffusion MRI

Fabio Nery[1] iD | **Filip Szczepankiewicz**[2,3,4] iD | **Leevi Kerkelä**[1] | **Matt G. Hall**[1,5] | **Enrico Kaden**[6] | **Isky Gordon**[1] | **David L. Thomas**[7,8] | **Chris A. Clark**[1]

[1]Developmental Imaging and Biophysics Section, UCL Great Ormond Street Institute of Child Health, London, United Kingdom

[2]Department of Radiology, Brigham and Women's Hospital, Boston, Massachusetts

[3]Harvard Medical School, Boston, Massachusetts

[4]Medical Radiation Physics, Clinical Sciences, Lund, Lund University, Lund, Sweden

[5]National Physical Laboratory, Teddington, United Kingdom

[6]Centre for Medical Image Computing, University College London, London, United Kingdom

[7]Leonard Wolfson Experimental Neurology Centre, UCL Queen Square Institute of Neurology, London, United Kingdom

[8]Department of Brain Repair and Rehabilitation, UCL Queen Square Institute of Neurology, London, United Kingdom

Correspondence
Fabio Nery, Developmental Imaging and Biophysics Section, UCL Great Ormond Street Institute of Child Health, 30 Guilford Street, London, WC1N 1EH, United Kingdom.
Email: fabio.nery.13@ucl.ac.uk

Funding information
Great Ormond Street Hospital Children's Charity, Grant/Award Number: V0318; NIHR Great Ormond Street Hospital Biomedical Research Centre; UCL Leonard Wolfson Experimental Neurology Centre, Grant/Award Number: PR/ylr/18575; NIH, Grant/Award Number: P41EB015902.

Purpose: To demonstrate the feasibility of multidimensional diffusion MRI to probe and quantify microscopic fractional anisotropy (µFA) in human kidneys in vivo.

Methods: Linear tensor encoded (LTE) and spherical tensor encoded (STE) renal diffusion MRI scans were performed in 10 healthy volunteers. Respiratory triggering and image registration were used to minimize motion artefacts during the acquisition. Kidney cortex–medulla were semi-automatically segmented based on fractional anisotropy (FA) values. A model-free analysis of LTE and STE signal dependence on b-value in the renal cortex and medulla was performed. Subsequently, µFA was estimated using a single-shell approach. Finally, a comparison of conventional FA and µFA is shown.

Results: The hallmark effect of µFA (divergence of LTE and STE signal with increasing b-value) was observed in all subjects. A statistically significant difference between LTE and STE signal was found in the cortex and medulla, starting from $b = 750$ s/mm^2 and $b = 500$ s/mm^2, respectively. This difference was maximal at the highest b-value sampled ($b = 1000$ s/mm^2) which suggests that relatively high b-values are required for µFA mapping in the kidney compared to conventional FA. Cortical and medullary µFA were, respectively, 0.53 ± 0.09 and 0.65 ± 0.05, both respectively higher than conventional FA (0.19 ± 0.02 and 0.40 ± 0.02).

Conclusion: The feasibility of combining LTE and STE diffusion MRI to probe and quantify µFA in human kidneys is demonstrated for the first time. By doing so, we show that novel microstructure information—not accessible by conventional diffusion encoding—can be probed by multidimensional diffusion MRI. We also identify relevant technical limitations that warrant further development of the technique for body MRI.

1 | INTRODUCTION

Diffusion tensor imaging (DTI) is a widely used diffusion-weighted imaging approach that has been successful because of its sensitivity to changes in tissue microstructure. However, tissue that is heterogeneous on a sub-voxel scale cannot be fully captured by the single diffusion tensor in DTI, meaning that the information on microscopic anisotropy and orientation dispersion is lost. The problem is not solely because of poor signal representation or tissue modelling but depends also on the diffusion encoding technique itself. If an acquisition is limited to a single diffusion encoding b-tensor shape, such as conventional linear tensor encoding (LTE), situations arise where vastly different tissue structures may yield virtually identical signal behavior.[1-3] In this setting, fractional anisotropy (FA) estimates are confounded by microscopic anisotropy and orientation dispersion, making their interpretation ambiguous.[4,5] Rotation invariant diffusion data (whose signal attenuation does not vary on rotations) can be acquired using isotropic diffusion encoding[6,7] (also referred to as spherical tensor encoding [STE][8]). Recent advances in the design of multidimensional diffusion MRI (MD-dMRI) acquisition schemes,[9] including the use of optimized gradient waveforms,[10] have enabled efficient spherical tensor encoding (STE) on clinical systems.[3] A joint analysis of LTE and STE provides more specific information on the underlying distribution of diffusion tensors compared to what is possible using LTE alone, allowing the effects of microscopic anisotropy and orientation dispersion to be disentangled and therefore to measure microscopic diffusion anisotropy (µFA) independently of orientation dispersion.[2,11-13] More generally, µFA can be probed in acquisitions where diffusion encoding is performed using measurement b-tensors with different shapes.[8,9] In addition to STE, double-diffusion encoding methods,[14-19] which encode diffusion along 2 directions before readout, provide planar b-tensors that also allow quantification of µFA.[20] Contrast-agent free quantitative biomarkers are actively being sought-after in the field of renal MRI.[21-25] In diffusion tensor imaging (DTI),[26] FA has been widely used in the kidneys as a non-invasive probe of tubular integrity[22,27] and the geometric arrangement of microscopic structure. Several studies consistently demonstrate a greater degree of anisotropy in the kidney medulla compared to the cortex (Kataoka et al,[28] Kido et al,[29] and Chan et al,[30] among others). A significant decrease in FA has been found in chronic kidney disease patients compared to healthy controls.[31] Furthermore,

DTI has been used to assess renal allograft function early following transplantation[32] and has shown reduced medullary FA and FA-based cortico–medullary differentiation in renal transplant recipients with impaired allograft function compared to those with good or moderate function.[33] However, FA remains unable to differentiate between different pathophysiological mechanisms underlying renal dysfunction.[22] A recent study on pediatric renal allografts has shown a moderate correlation of medullary FA with several Banff histopathology scores (particularly at higher b-values) but not cortical FA.[34] Neither cortical nor medullary FA correlated with the glomerulitis (g) Banff score. This suggests that more specific biomarkers of renal microstructure are desirable. However, at the time of writing, and to the best of our knowledge, no studies have been reported investigating microscopic anisotropy in the renal parenchyma.[35,36] The aim of this work is to investigate, for the first time, the feasibility of using STE in combination with conventional LTE in the human kidney to probe and quantify tissue microscopic anisotropy in vivo. A detailed analysis of the LTE and STE diffusion-weighted signal in healthy subjects has been performed, followed by quantification of cortical and medullary µFA using a single-shell approach, along with a comparison to conventional FA, and an overview of current challenges in MD-dMRI of the kidneys.

2 | METHODS

Ten healthy volunteers (age 31 ± 6 y, 5 male) were scanned on a 3T Prisma MR system (Siemens Healthineers, Erlangen, Germany) using a prototype spin-echo sequence with EPI readout that facilitates diffusion encoding with variable b-tensor shapes (Figure 1). Data was acquired with LTE and STE using FOV = 288×288 mm^2, voxel size = $3 \times 3 \times (4\text{–}4.6)$ mm^3, 11 coronal oblique slices, TE = 87 ms; 3/4 partial-Fourier and parallel imaging in-plane acceleration R = 2 (GRAPPA). TR was 3000 ms (following a consensus recommendation)[37] to ensure significant T_1 recovery between volumes; the data acquisition window was limited to 1500 ms to reduce motion artefacts. Furthermore, setting the minimum TR to 3000 ms also minimizes the likelihood of triggering events not related to respiration (i.e., no more than 1 triggering event per respiratory cycle is allowed).[38] Diffusion data was acquired at 4 encoding strengths (b-values of 250, 500, 750, 1000 s/mm^2), each with 2 signal averages,
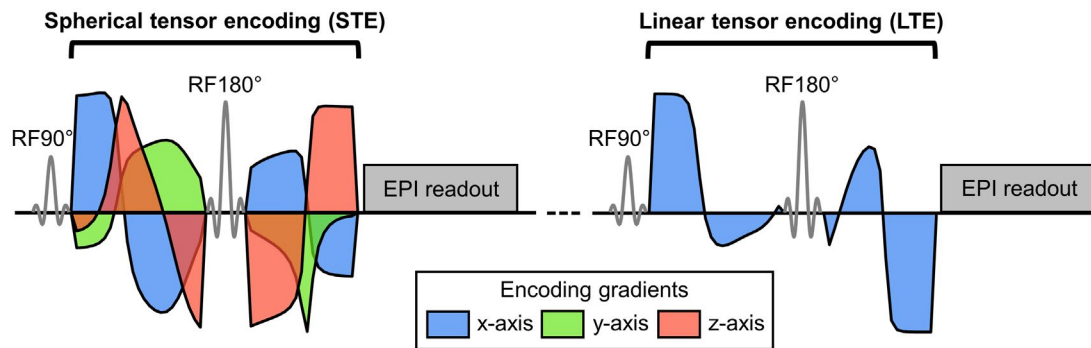
FIGURE 1 Schematic of the spin-echo EPI sequence with optimized gradient waveforms to yield spherical and linear *b*-tensor encoding (STE and LTE).[10] Note that STE and LTE measurements are performed separately (i.e., require separate RF excitation pulses)

in addition to a non-diffusion-weighted reference scan ($b = 0$ s/mm^2) repeated 4 times. The number of encoding directions was chosen such that a rotation invariant powder signal could be obtained with the acquisition protocol. The minimum number of directions necessary to fulfil this requirement was estimated by following a previously proposed simulation framework.[39] Most renal DTI studies have found FA in the renal medulla to be (1) lower than 0.5, and (2) higher than cortical FA (see above). Therefore, assuming a maximum FA of 0.5 (see Results for details of our FA estimates in this data set), ~11 directions yield a rotation invariant powder signal for $b \times$ MD < 3,[39] where MD = mean diffusivity. As such, considering the highest b-value used in this study (1000 s/mm^2), ~11 directions yield a rotation invariant powder signal for a MD of 3×10^{-3} mm^2/s (diffusion coefficient of water at body temperature),[40] which is above the typically observed MD in the renal cortex and medulla[41-43] (also verified in our data, see Results). The number of encoding directions was therefore set to 12 for all LTE and STE acquisitions. Encoding waveforms were optimized numerically[10] assuming a maximum gradient amplitude of 75 mT/m and slew rate of 100 T/m/s, heat dissipation factor η = 0.6, and using the Euclidean norm to obtain rotatable waveforms[39] (Figure 1). The LTE waveform was generated from the STE waveform such that the magnitude of the *q*-vector remained constant.[44,45] Respiratory triggering (at end-expiration) was used. Experience with respiratory-triggered acquisitions on our system suggests that using a short trigger delay increases the likelihood of the initial portion of the image readout occurring during the quiescent part of the respiratory cycle. This is consistent with a previous study.[28] The respiratory triggering parameters used in this work were threshold 20% and trigger delay 200 ms. The nominal scan time (i.e., without accounting for the delays associated with respiratory triggering) was 11 min 00 s (5 min 30 s for each of the encoding schemes). The time penalty associated with using respiratory triggering compared to non-triggered acquisitions was investigated (see Results). Retrospective motion correction (image registration) of individual diffusion-weighted volumes to the reference $b = 0$ s/mm^2

data before powder averaging was performed separately for each kidney using elastix.[46] The whole kidney parenchyma (excluding the renal hilum) was manually segmented in the mean $b = 0$ s/mm^2 image. To reduce operator bias, subsequent cortical–medullary regions of interest (ROIs) were segmented using an automatic algorithm developed in-house. Briefly, it uses Gaussian mixture modeling to determine an optimal subject-wise threshold to separate cortex from medulla based on conventional FA voxel-wise estimates (Figure 2), followed by a 2D morphological opening operation to remove spurious voxels in the resulting ROIs. Multi-shell diffusion tensor fitting was performed with FSL[47] to obtain voxel-wise conventional FA and MD estimates using all b-values in the LTE data set. Quantification of µFA was performed using a single-shell approach, using the highest sampled b-value (1000 s/mm^2) with the following equation (see Lasič et al[2])

$$\mu FA = \sqrt{\frac{3}{2} \left(1 + \frac{2}{5} \cdot \frac{1}{\Delta \tilde{\mu}_2} \right)^{-\frac{1}{2}}}. \quad (1)$$

where $\Delta \tilde{\mu}_2$, the difference in scaled variance of apparent diffusion coefficients, is given by

$$\Delta \tilde{\mu}_2 = \ln \frac{E_{LTE}}{E_{STE}} 2 \bar{D}^{-2} b^{-2}. \quad (2)$$

where E_{LTE} and E_{STE} are, respectively, the powder-averaged LTE and STE signal normalized to the $b = 0$ s/mm^2 reference scan, $\bar{D}$ is the mean diffusivity and b is the encoding strength. First, the feasibility of voxel-wise µFA mapping was assessed by determining the proportion of voxels for which µFA could be not quantified (i.e., because of a negative LTE-STE difference). Subsequently, to maximize the SNR of the LTE-STE difference and therefore the reliability of the µFA estimation, a ROI-based approach was used. Here, LTE and STE powder averaged signal was separately averaged within the cortical and medullary ROIs before µFA quantification in each tissue type and in all subjects.
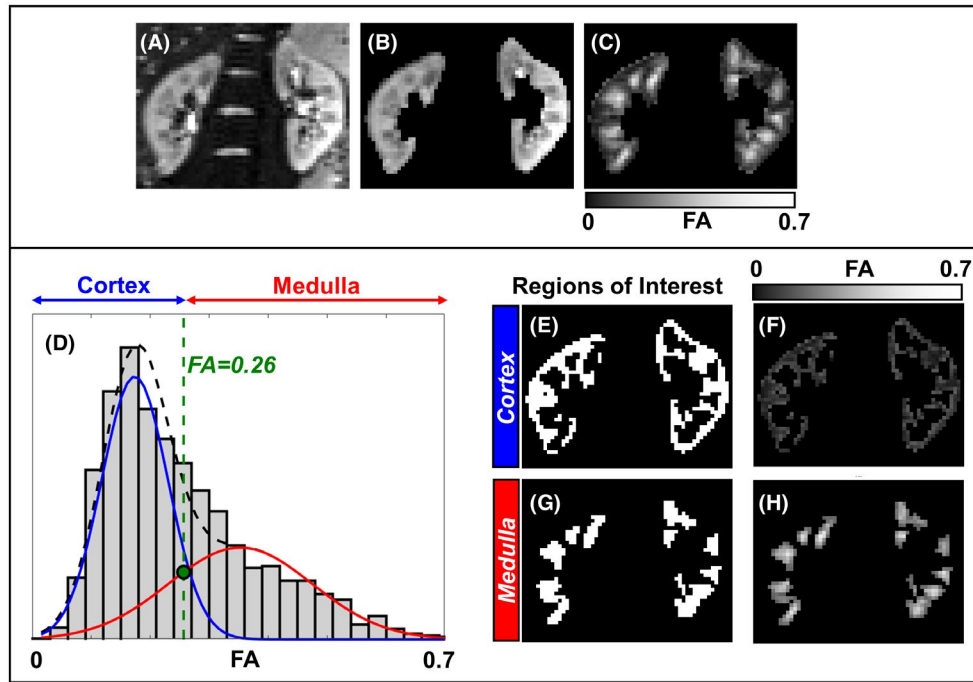
FIGURE 2 Fractional anisotropy (FA)-based automatic segmentation of cortex and medulla on a single representative subject (after manual segmentation of kidney parenchyma to exclude the hilum). A Gaussian mixture model (2 components) is fitted to the histogram of the FA values of the kidney parenchyma (obtained from the LTE acquisition) and a FA threshold to separate cortex from medulla is obtained from the intersection of the 2 resulting Gaussian distributions (green marker and dashed line). Note that the value of the FA threshold indicated in this figure is specific for this particular subject. Even though a single central slice is shown, 3 central slices are used to obtain the FA histogram and subsequent regions of interest (ROIs). (A) Non-diffusion weighted ($b = 0$ s/mm^2) image. (B) Cropped renal parenchyma on the $b = 0$ s/mm^2 image. (C) FA map. (D) FA intensity histogram and result of Gaussian mixture model fitting and subsequent estimation of the FA threshold to segment cortex–medulla. (E) Cortical ROIs. (F) Masked cortex in the FA map. (G) Medulla ROI. (H) Masked medulla in the FA map

3 | RESULTS

Based on visual inspection of SNR and image artefacts, all LTE and STE data had sufficiently high quality for analysis, and the 3 central slices from each subject were used for all further analyses. The true scan time (both encoding schemes), including delays because of respiratory triggering and subject-specific respiratory rates was 17 ± 4 min (average $\pm$ SD). Respiratory triggering significantly increased scan time (approximately doubling it in 1 subject) compared to a non-triggered acquisition. However, respiratory triggering has been shown to improve data quality in DTI of native kidneys even when image registration is used[48] which motivated its use in this study. The conventional FA threshold calculated via Gaussian mixture modeling to differentiate cortex from medulla was 0.28 ± 0.02 (mean $\pm$ SD across all subjects). All cortical and medullary ROIs obtained by the proposed segmentation approach were reviewed by 2 authors with 5 and 35 y of experience in renal imaging (the latter being a radiologist) and were deemed anatomically accurate (see Figure 2E-H for an example on a representative subject). This supports the initial assumption that FA could be used to separate cortex and medulla (at least in healthy kidneys).

This is consistent with most renal DTI publications that have demonstrated medullary FA to be significantly higher than cortical FA in healthy volunteers.[22] The FA estimates using the resulting ROIs were 0.19 ± 0.02 and 0.40 ± 0.03, respectively, for kidney cortex and medulla. Mean cortical and medullary MD were, respectively, $1.84 \times 10^{-3} \pm 0.08 \times 10^{-3}$ mm^2/s and $1.77 \times 10^{-3} \pm 0.09 \times 10^{-3}$ mm^2/s (2-tailed paired t-test, $P < 5 \times 10^{-4}$), also reflecting the expected higher diffusivity in the renal cortex compared to the medulla in healthy subjects.[22] Figure 3A and B show the dependence of the LTE and STE powder average signal, and the normalized signal difference (i.e., (Signal(LTE) − Signal(STE))/Signal(LTE)), on b-value for medulla and cortical ROIs averaged across the 10 subjects. The hallmark of microscopic anisotropy (µFA > 0) is divergence of the STE and LTE signals with increasing b-value.[2] Figure 3B highlights the clear trend of increasing relative difference between the LTE and STE signals with increasing b-value in both kidney parenchyma regions (cortex and medulla). This effect was observed individually in each of the subjects (see Supporting Information Table S1). Statistically significant LTE-STE signal differences (two-tailed paired t-test, $P < 0.05$) were found from $b = 500$ s/mm^2 in the medulla and $b = 750$ s/mm^2 in the
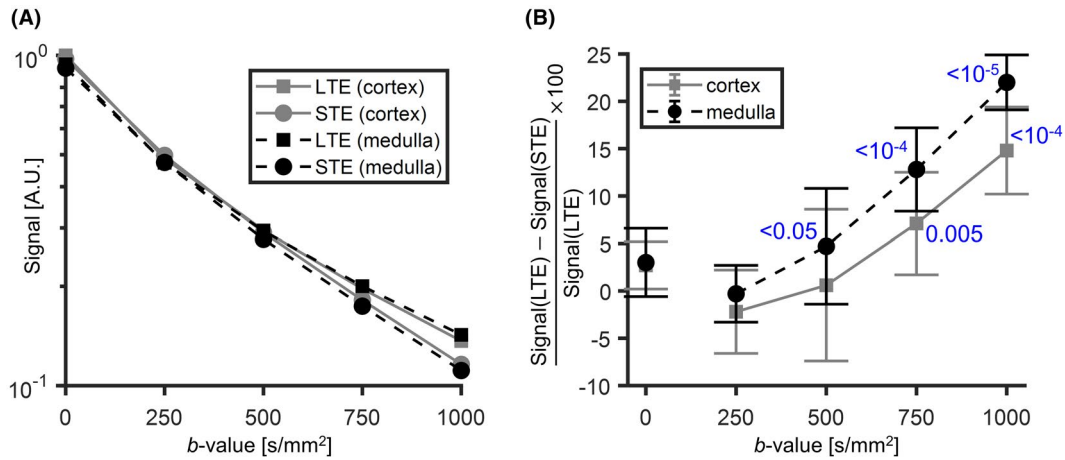
FIGURE 3 (A) Signal versus b-value averaged across 10 subjects within cortical and medullary regions of interest (ROIs). (B) Highlights the trend of increasing relative difference between the LTE and the STE signal with increasing b-value. The P-value corresponding to the statistically significant differences between the LTE and the STE signal is shown in blue (2-tailed paired t-test)

cortex. The relative LTE-STE difference was greatest at $b = 1000$ s/mm^2 (the highest b-value sampled in this study) for both medulla ($22 \pm 3\%$; $P < 10^{-5}$) and cortex ($15 \pm 5\%$; $P < 10^{-4}$) (see Supporting Information Table S1). This suggests that relatively high b-values (compared to most renal DTI studies) are required to capture microscopic anisotropy information in the kidneys, particularly in the cortex. Figure 4 shows a comparison of conventional FA and LTE-STE relative difference maps with increasing b-value on a single representative subject. Excellent cortico–medullary differentiation is seen in the FA maps, whereas the LTE-STE relative difference is shown with a more homogenous intensity distribution throughout the renal parenchyma. In our voxel-wise analysis, a lack of divergence of LTE and STE signal consistent with the hallmark of μFA (i.e., a positive LTE-STE difference) resulted in a failure to estimate μFA using the single-shell method in a non-trivial proportion of voxels ($5 \pm 9\%$ in the cortex and $2 \pm 4\%$ in the medulla [median $\pm$ interquartile range]). Across all subjects, ROI-based cortical and medullary μFA were, respectively, 0.53 ± 0.09 and 0.65 ± 0.05 (two-tailed paired t-test, $P < 10^{-4}$) (individual results for each subject shown in Supporting Information Table S2). Furthermore, μFA was shown to be significantly larger than conventional FA in both the cortex and medulla (2-tailed paired t-tests, $P < 10^{-5}$). Figure 5 shows a comparison of conventional FA and μFA maps in a central slice of 2 subjects. These are, respectively, examples of worst- and best-case scenarios in terms of image quality of the μFA maps (chosen on the basis of the highest and lowest proportion of μFA calculation fails in the cortex). The lower cortico-medullary differentiation in the μFA map compared to the standard FA in Figure 5 (mostly because of higher μFA vs. standard FA in the cortex) suggests that orientation dispersion in the cortex enhances the cortico–medullary differentiation seen in conventional DTI FA measures.

4 | DISCUSSION

This work provides evidence that MD-dMRI methods are capable of probing microscopic anisotropy in the human kidneys in vivo and provides information on the lower bounds of the range of b-values required to map it. Similarly to previous studies,[48,49] the use of retrospective image registration improved data quality by reducing motion artefacts and enhancing the cortico–medullary differentiation. The hallmark effect of microscopic anisotropy (divergence between LTE and STE signal with increasing b-value) is demonstrated in the renal cortex and more predominantly in the medulla without the need for any model assumptions or fitting. Mapping μFA in the kidneys in a voxel-wise manner was found challenging in a subset of subjects, particularly in patches of cortical tissue (as shown in Figure 5). This is consistent with previous work outside the kidneys that has shown estimation of μFA to be problematic in tissue with low intrinsic μFA.[2,45] This was a minor issue in the medulla with <5% of μFA calculation failures in the majority of subjects (see Supporting Information Table S2). Nevertheless, to overcome this, we resorted to a ROI-based approach where quantification of μFA in all subjects in both cortex and medulla was successful. One might hypothesize use of μFA to help elucidate the pathophysiological mechanisms that decrease diffusion anisotropy in the kidneys.[33,50] Indeed, where orientation dispersion is a plausible feature of tissue microstructure (e.g., convoluted tubules), μFA may provide a more accurate assessment of microstructural integrity compared to conventional FA. This hypothesis will require future clinical studies, whereas the present study focused on establishing the feasibility of measuring μFA and obtaining baseline data from healthy volunteers. Several limitations must be addressed in future research. First, the waveforms used here are not compensated with
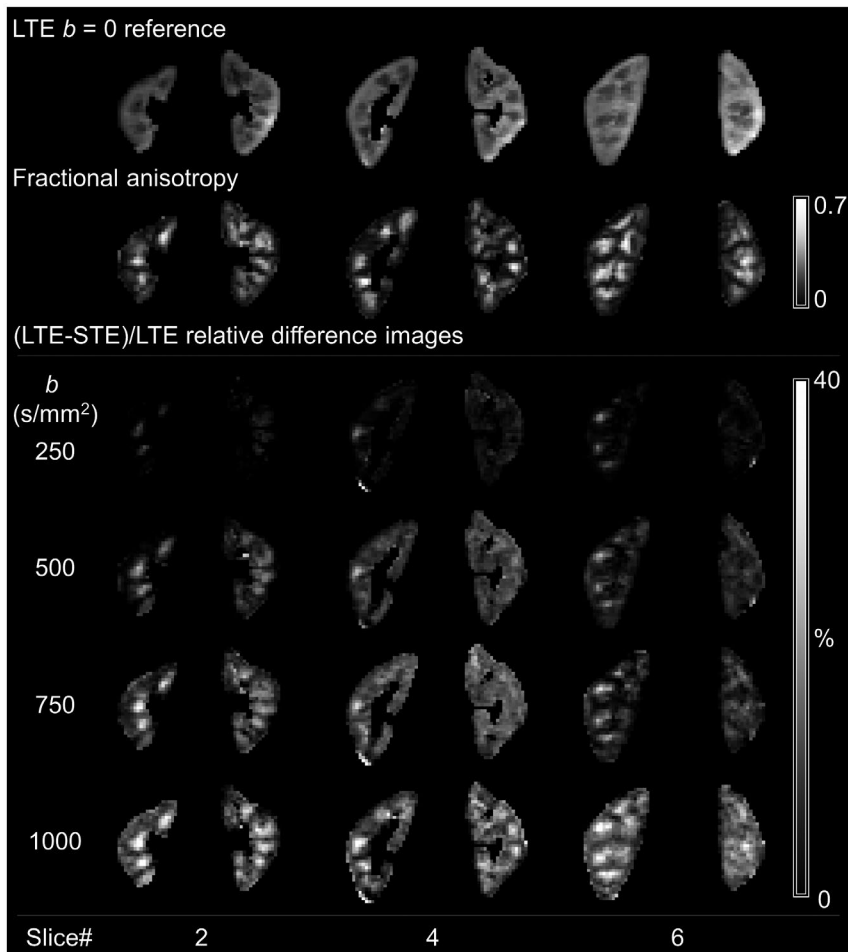
FIGURE 4 Non-diffusion-weighted (top), fractional anisotropy (FA) and LTE-STE relative difference images in 3 kidney slices of 1 subject (slice 2: anterior; slice 4: central; slice 6: posterior). The relative difference images are shown with a constant intensity scale across all b-values (ranging from 0–40%)
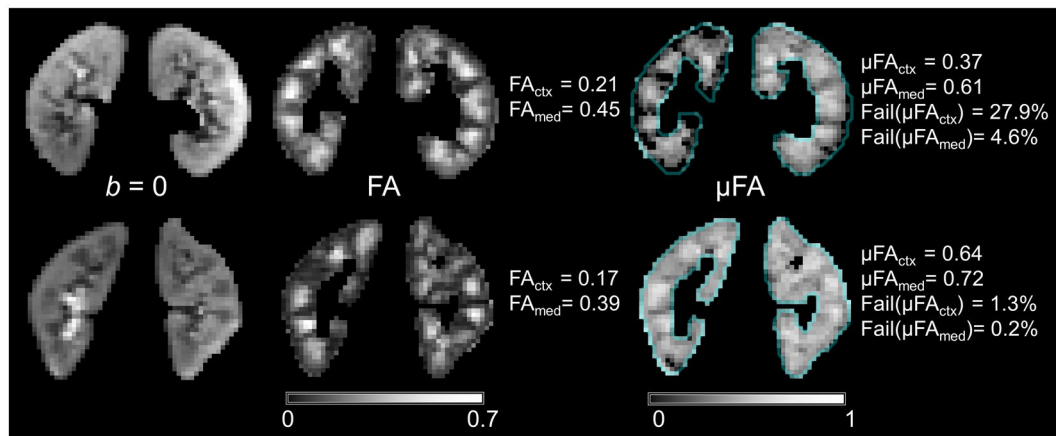

FIGURE 5 Central slice $b = 0$ s/mm^2 reference image, conventional FA map and µFA map (left to right) for 2 subjects (rows, respectively the worst and best-case scenarios as judged by the proportion of cortical µFA calculation failures across the 10 subjects). Both conventional FA and µFA range from [0, 1]. However, for figure displaying purposes the intensity range of the conventional FA map is set to [0, 0.7]. Note that the $b = 0$ s/mm^2 image shows the whole kidneys whereas for both quantitative maps the hilum was removed to avoid biasing any FA or µFA estimates. An artificial boundary (cyan) depicting the boundary of the kidneys (excluding hilum) was added to the µFA map for easy visualization of voxels where µFA calculation was not possible (shown as dark regions in the grayscale color map). Note that even though voxel-wise calculations of µFA were necessary to generate the maps in this figure, the reported µFA values (text) were obtained using the ROI-based approach. See results for all subjects in Supporting Information Table S2

respect to concomitant fields that may cause a hyper-attenuation of the STE and potentially yield overestimation of the LTE-STE difference signal as recently reported.[51] Second, the contribution of flow on anisotropy measures has not been investigated in this work. This would be required to disentangle fast pseudo-diffusion effects due to microscopic capillary and/or tubular flow from passive diffusion effects from which tissue microstructure properties can be estimated. This is especially relevant in the kidneys and in the cortex in particular where one might expect the convoluted tubule (through which flow is significant) to be a candidate for locally anisotropic diffusion. Using flow-compensation techniques may provide the additional benefit of compensating for spin dephasing (and therefore signal loss) due to bulk motion effects which may improve image quality.[52] Furthermore, a potential limitation is that LTE and STE waveforms were not matched with respect to the diffusion time, which may cause a parameter bias in systems with diffusion time dependencies.[53] An investigation of time-dependency of our diffusion measurements was beyond the scope of this work and is frequently overlooked in the renal diffusion MR literature. Our estimate for mean diffusivity ($\sim 1.8 \times 10^{-3}$ mm^2/s) suggests mean displacements of $\sim$11–16 μm for diffusion times on the order of 35–70 ms (note the time elapsed between the start and end of the diffusion encoding gradients is $\sim$70 ms). The tubular diameters within the human kidney nephron components range in sizes from 10–70 μm (tubular diameter).[54,55] Therefore, an overlap between the sizes of the diffusion-restricting structures and the diffusion propagator is expected to a considerable extent. This suggests that a diffusion-time dependency (i.e., mean diffusivity not being independent from the gradient waveform) is likely to exist and this should be investigated in future studies. Finally, for clinical applications where scan time is limited, optimization of parsimonious time-efficient protocols is warranted.

5 | CONCLUSION

This work demonstrates the technical feasibility of tensor-valued diffusion encoding for renal imaging and provides pilot data to demonstrate the minimum b-values required to probe microscopic fractional anisotropy. We then harness this information to provide the first estimation for microscopic anisotropy in human kidney in vivo. Finally, we highlight current limitations, motivating further investigation of the microstructural information offered by multidimensional diffusion MRI for renal applications. This approach may ultimately enable a more specific in vivo characterization of the microstructure of human kidney in healthy and diseased subjects, compared to methods based on conventional diffusion encoding.

ORCID

Fabio Nery 🔟 https://orcid.org/0000-0002-4220-0997
Filip Szczepankiewicz 🔟 https://orcid.org/0000-0002-5251-587X

REFERENCES

1. Mitra PP. Multiple wave-vector extensions of the NMR pulsed-field-gradient spin-echo diffusion measurement. *Phys Rev B*. 1995;51:15074–15078.
2. Lasič S, Szczepankiewicz F, Eriksson S, Nilsson M, Topgaard D. Microanisotropy imaging: quantification of microscopic diffusion anisotropy and orientational order parameter by diffusion MRI with magic-angle spinning of the q-vector. *Front Phys*. 2014;2:1–14.
3. Szczepankiewicz F, Lasič S, van Westen D, et al. Quantification of microscopic diffusion anisotropy disentangles effects of orientation dispersion from microstructure: applications in healthy volunteers and in brain tumors. *NeuroImage*. 2015;104:241–252.
4. Beaulieu C. The basis of anisotropic water diffusion in the nervous system – a technical review. *NMR Biomed*. 2002;15:435–455.
5. Jeurissen B, Leemans A, Tournier JD, Jones DK, Sijbers J. Investigating the prevalence of complex fiber configurations in white matter tissue with diffusion magnetic resonance imaging. *Hum Brain Mapp*. 2013;34:2747–2766.
6. Mori S, Van Zijl P. Diffusion weighting by the trace of the diffusion tensor within a single scan. *Magn Reson Med*. 1995;33:41–52.
7. Wong EC, Cox RW, Song AW. Optimized isotropic diffusion weighting. *Magn Reson Med*. 1995;34:139–143.
8. Westin C-F, Knutsson H, Pasternak O, et al. Q-space trajectory imaging for multidimensional diffusion MRI of the human brain. *NeuroImage*. 2016;135:345–362.
9. Topgaard D. Multidimensional diffusion MRI. *J Magn Reson*. 2017;275:98–113.
10. Sjölund J, Szczepankiewicz F, Nilsson M, Topgaard D, Westin CF, Knutsson H. Constrained optimization of gradient waveforms for generalized diffusion encoding. *J Magn Reson*. 2015;261:157–168.
11. Cory DG, Garroway AN, Miller JB. Applications of spin transport as a probe of local geometry. *Polymer Prepr*. 1990;31:149–150.
12. Shemesh N, Özarslan E, Komlosh ME, Basser PJ, Cohen Y. From single-pulsed field gradient to double-pulsed field gradient MR: gleaning new microstructural information and developing new forms of contrast in MRI. *NMR Biomed*. 2010;23:757–780.
13. Lawrenz M, Finsterbusch J. Double-wave-vector diffusion-weighted imaging reveals microscopic diffusion anisotropy in the living human brain. *Magn Reson Med*. 2013;69:1072–1082.
14. Callaghan PT, Komlosh ME. Locally anisotropic motion in a macroscopically isotropic system: displacement correlations measured

using double pulsed gradient spin-echo NMR. *Magn Reson Chem*. 2002;40:S15–S19.

15. Özarslan E, Basser PJ. Microscopic anisotropy revealed by NMR double pulsed field gradient experiments with arbitrary timing parameters. *J Chem Phys*. 2008;128:154511.

16. Shemesh N, Özarslan E, Adiri T, Basser PJ, Cohen Y. Noninvasive bipolar double-pulsed-field-gradient NMR reveals signatures for pore size and shape in polydisperse, randomly oriented, inhomogeneous porous media. *J Chem Phys*. 2010;133:044705.

17. Lawrenz M, Koch MA, Finsterbusch J. A tensor model and measures of microscopic anisotropy for double-wave-vector diffusion-weighting experiments with long mixing times. *J Magn Reson*. 2010;202:43–56.

18. Jespersen SN, Lundell H, Sønderby CK, Dyrby TB. Orientationally invariant metrics of apparent compartment eccentricity from double pulsed field gradient diffusion experiments. *NMR Biomed*. 2013;26:1647–1662.

19. Jensen JH, Hui ES, Helpern JA. Double-pulsed diffusional kurtosis imaging. *NMR Biomed*. 2014;27:363–370.

20. Yang G, Tian Q, Leuze C, Wintermark M, McNab JA. Double diffusion encoding MRI for the clinic. *Magn Reson Med*. 2018;80:507–520.

21. Wolf M, de Boer A, Sharma K, et al. Magnetic resonance imaging T1- and T2-mapping to assess renal structure and function: a systematic review and statement paper. *Nephrol Dial Transplant*. 2018;33(suppl_2):ii41-ii50.

22. Caroli A, Schneider M, Friedli I, et al. Diffusion-weighted magnetic resonance imaging to assess diffuse renal pathology: a systematic review and statement paper. *Nephrol Dial Transplant*. 2018;33(suppl_2):ii29–ii40.

23. Odudu A, Nery F, Harteveld AA, et al. Arterial spin labelling MRI to measure renal perfusion: a systematic review and statement paper. *Nephrol Dial Transplant*. 2018;33(suppl_2):ii15–ii21.

24. Nery F, Gordon I, Thomas DL. Non-invasive renal perfusion imaging using arterial spin labeling MRI: challenges and opportunities. *Diagnostics*. 2018;8:2.

25. Pruijm M, Mendichovszky IA, Liss P, et al. Renal blood oxygenation level-dependent magnetic resonance imaging to measure renal tissue oxygenation: a statement paper and systematic review. *Nephrol Dial Transplant*. 2018;33(suppl_2):ii22–ii28.

26. Basser PJ, Mattiello J, LeBihan D. MR diffusion tensor spectroscopy and imaging. *Biophys J*. 1994;66:259–267.

27. Gaudiano C, Clementi V, Busato F, et al. Renal diffusion tensor imaging: is it possible to define the tubular pathway? A case report. *Magn Reson Imaging*. 2011;29:1030–1033.

28. Kataoka M, Kido A, Yamamoto A, et al. Diffusion tensor imaging of kidneys with respiratory triggering: optimization of parameters to demonstrate anisotropic structures on fraction anisotropy maps. *J Magn Reson Imaging*. 2009;29:736–744.

29. Kido A, Kataoka M, Yamamoto A, et al. Diffusion tensor MRI of the kidney at 3.0 and 1.5 Tesla. *Acta Radiol*. 2010;51:1059–1063.

30. Chan RW, Von Deuster C, Stoeck CT, et al. High-resolution diffusion tensor imaging of the human kidneys using a free-breathing, multi-slice, targeted field of view approach. *NMR Biomed*. 2014;27:1300–1312.

31. Liu Z, Xu Y, Zhang J, et al. Chronic kidney disease: pathological and functional assessment with diffusion tensor imaging at 3T MR. *Eur Radiol*. 2015;25:652–660.

32. Fan W-J, Ren T, Li Q, et al. Assessment of renal allograft function early after transplantation with isotropic resolution diffusion tensor imaging. *Eur Radiol*. 2016;26:567–575.

33. Lanzman RS, Ljimani A, Pentang G, et al. Kidney transplant: functional assessment with diffusion-tensor MR imaging at 3T. *Radiology*. 2013;266:218–225.

34. Li Y, Lee MM, Worters PW, MacKenzie JD, Laszik Z, Courtier JL. Pilot study of renal diffusion tensor imaging as a correlate to histopathology in pediatric renal allografts. *AJR Am J Roentgenol*. 2017;208:1358–1364.

35. Nery F, Hall MG, Thomas DL, et al. Microscopic diffusion anisotropy imaging in the kidneys. In *Proceedings of the 26th Annual Meeting of ISMRM*, Paris, France, 2018. Abstract 5232.

36. Nery F, Szczepankiewicz F, de Almeida Martins JP, et al. Investigating microscopic diffusion anisotropy in human kidney using multidimensional diffusion encoding. In *Proceedings of the 27th Annual Meeting of ISMRM*, Montreal, Canada, 2019. Abstract 3524.

37. Taouli B, Beer AJ, Chenevert T, et al. Diffusion-weighted imaging outside the brain: consensus statement from an ISMRM-sponsored workshop. *J Magn Reson Imaging*. 2016;44:521–540.

38. Binser T, Thoeny HC, Eisenberger U, Stemmer A, Boesch C, Vermathen P. Comparison of physiological triggering schemes for diffusion-weighted magnetic resonance imaging in kidneys. *J Magn Reson Imaging*. 2010;31:1144–1150.

39. Szczepankiewicz F, Sjölund J, Ståhlberg F, Lätt J, Nilsson M. Whole-brain diffusional variance decomposition (DIVIDE): demonstration of technical feasibility at clinical MRI systems. arXiv preprint arXiv 2016:1612.06741.

40. Le Bihan D, Iima M. Diffusion magnetic resonance imaging: what water tells us about biological tissues. *PLoS Biol*. 2015;13:e1002203.

41. Sigmund EE, Vivier P-H, Sui D, et al. Intravoxel incoherent motion and diffusion-tensor imaging in renal tissue under hydration and furosemide flow challenges. *Radiology*. 2012;263:758–769.

42. Chuck NC, Steidle G, Blume I, Fischer MA, Nanz D, Boss A. Diffusion tensor imaging of the kidneys: influence of b-value and number of encoding directions on image quality and diffusion tensor parameters. *J Clin Imaging Sci*. 2013;3:53.

43. Hilbert F, Wech T, Neubauer H, Veldhoen S, Bley TA, Köstler H. Comparison of turbo spin echo and echo planar imaging for intravoxel incoherent motion and diffusion tensor imaging of the kidney at 3 Tesla. *Z Med Phys*. 2017;27:193–201.

44. Eriksson S, Lasic S, Topgaard D. Isotropic diffusion weighting in PGSE NMR by magic-angle spinning of the q-vector. *J Magn Reson*. 2013;226:13–18.

45. Szczepankiewicz F, van Westen D, Englund E, et al. The link between diffusion MRI and tumor heterogeneity: mapping cell eccentricity and density by diffusional variance decomposition (DIVIDE). *NeuroImage*. 2016;142:522–532.

46. Klein S, Staring M, Murphy K, Viergever MA, Pluim J. elastix: a toolbox for intensity-based medical image registration. *IEEE Trans Med Imaging*. 2010;29:196–205.

47. Smith SM, Jenkinson M, Woolrich MW, et al. Advances in functional and structural MR image analysis and implementation as FSL. *NeuroImage*. 2004;23(Suppl1):S208–S219.

48. Seif M, Mani LY, Lu H, et al. Diffusion tensor imaging of the human kidney: does image registration permit scanning

without respiratory triggering? *J Magn Reson Imaging*. 2016;44: 327–334.

49. Seif M, Lu H, Boesch C, Reyes M, Vermathen P. Image registration for triggered and non-triggered DTI of the human kidney: reduced variability of diffusion parameter estimation. *J Magn Reson Imaging*. 2015;41:1228–1235.

50. Hueper K, Hartung D, Gutberlet M, et al. Magnetic resonance diffusion tensor imaging for evaluation of histopathological changes in a rat model of diabetic nephropathy. *Invest Radiol*. 2012;47:430–437.

51. Szczepankiewicz F, Westin CF, Nilsson M. Maxwell-compensated design of asymmetric gradient waveforms for tensor-valued diffusion encoding. *Magn Reson Med*. 2019. https://doi.org/10.1002/mrm.27828.

52. Haacke EM, Lenz GW. Improving MR image quality in the presence of motion by using rephasing gradients. *AJR Am J Roentgenol*. 1987;148:1251–1258.

53. Lundell H, Nilsson M, Dyrby TB, et al. Microscopic anisotropy with spectrally modulated q-space trajectory encoding. In *Proceedings of the 25th Annual Meeting of ISMRM*, Honolulu, HI, 2017. Abstract 1086.

54. Taal MW, Chertow GM, Marsden PA, Skorecki K, Yu A, Brenner BM. *Brenner & Rector's the kidney*. 9th ed. Philadelphia, PA: Saunders Elsevier; 2011. 3064 p.

55. Xie L, Bennett KM, Liu C, Johnson GA, Zhang JL, Lee VS. MRI tools for assessment of microstructure and nephron function of the kidney. *Am J Physiol Renal Physiol*. 2016;311:F1109–F1124.

SUPPORTING INFORMATION

Additional supporting information may be found online in the Supporting Information section at the end of the article.

TABLE S1 Relative signal difference (%) between LTE and STE signal in cortical and medullary ROIs, for all b-values and subjects, calculated as $((S_{LTE} - S_{STE})/S_{LTE}) \times 100$, where S_{LTE} and S_{STE} are, respectively, the mean LTE and STE signal in the ROIs. The last row shows the *P*-value row corresponding to the differences between the LTE and the STE signal (2-tailed paired t-test). Significant differences ($P < 0.05$) are underlined

TABLE S2 Percentage of voxels for which μFA calculation was not possible (μFA "fails"). ROI-based μFA and conventional FA results shown individually for all subjects, for cortex and medulla